Energy & Environmental Science

ROYAL SOCIETY OF CHEMISTRY

PAPER

View Article Online
View Journal

Cite this: DOI: 10.1039/d0ee02276d

Operando X-ray spectroscopy visualizing the chameleon-like structural reconstruction on an oxygen evolution electrocatalyst†

Dengfeng Cao,‡[a] Daobin Liu,‡[ab] Shuangming Chen,‡[a] Oyawale Adetunji Moses,[a] Xingjia Chen,[a] Wenjie Xu,[a] Chuanqiang Wu,[a] Lirong Zheng,[c] Shengqi Chu,[c] Hongliang Jiang,[ad] Changda Wang,[a] Binghui Ge,[ef] Xiaojun Wu,[a] Jing Zhang[c] and Li Song *[a]

Received 18th July 2020,
Accepted 20th October 2020

DOI: 10.1039/d0ee02276d

rsc.li/ees

The ambiguous mechanism of electrocatalysts for the oxygen evolution reaction (OER) greatly hinders their industrial applications toward renewable and clean energy conversion. Here, we elaborately prepared a cobalt sulfide catalyst to perform a comprehensive study of the OER performance under neutral/alkaline conditions. The combination of synchrotron-based *operando* X-ray spectroscopic investigations and electron microscopy observations captured a chameleon-like structural self-optimization on the cobalt sulfide oxygen evolution electrocatalyst in both neutral and alkaline electrolytes. Driven by the actual working conditions (pH gradient, electrical potential, *etc.*), distinct catalytic sites could be activated dramatically. In particular, the CoOOH supported on a single-walled carbon nanotube (CoOOH-SWCNT) with residual S species was identified as the true catalyst under alkaline conditions rather than the entirely transformed CoOOH-SWCNT, while the oxygenated CoS-SWCNT (O-CoS-SWCNT) was formed as the true catalyst under neutral conditions. Undoubtedly, such a mechanism of opening different locks with different keys and its microstructural advantages together guarantee the high catalytic activity in different electrolytes. This work provides a promising catalyst as well as sheds light on the very essence of the structural self-optimization process of catalysts. It makes a significant contribution to the advancement of OER relevant studies in the future while providing new ideas for the fields of chemistry and catalysis.

Broader context

Electrocatalytic oxygen evolution reaction (OER), as the most fundamental process, is involved in a series of energy conversion processes, including water splitting, carbon dioxide (CO_2) reduction, rechargeable metal–air batteries, and regenerative fuel cells. Understanding catalytic processes and identifying active sites explicitly are pivotal for clarifying the catalytic mechanism and facilitating the development of advanced electrocatalysts. Here, systematical characterizations combined with *operando* X-ray absorption fine structure (XAFS) spectra visualized that the Co_9S_8-SWCNT catalyst underwent a chameleon-like structural reconstruction in different electrolytes. This work sheds light on the very essence of the structural self-optimization process of catalysts and further provides an in-depth insight into the catalytic mechanism for guiding the rational design of advanced catalysts.

[a] *National Synchrotron Radiation Laboratory, Hefei National Laboratory for Physical Sciences at the Microscales, Synergetic Innovation of Quantum Information & Quantum Technology, CAS Key Laboratory of Materials for Energy Conversion, CAS Center for Excellence in Nanoscience, Department of Materials Sciences and Engineering, University of Science and Technology of China, Hefei, Anhui 230026, China. E-mail: song2012@ustc.edu.cn*
[b] *School of Materials Science and Engineering, Nanyang Technological University, Singapore 639798, Singapore*
[c] *Institute of High Energy Physics, Chinese Academy of Sciences, Beijing, 100049, China*
[d] *School of Chemical Engineering, East China University of Science and Technology, Shanghai 200237, China*
[e] *Institute of Physical Science and Information Technology, Anhui University, Hefei 230601, China*
[f] *Beijing National Laboratory for Condensed Matter Physics, Institute of Physics, Chinese Academy of Science, Beijing 100190, China*

† Electronic supplementary information (ESI) available. See DOI: 10.1039/d0ee02276d

‡ These authors contributed equally to this work.

Introduction

Electrocatalysis is a greatly important way to realize the highly efficient and sustainable energy conversion such that it is developing rapidly to meet the dual challenges of the depletion of legacy fossil fuels and the associated environmental contamination from burning such fossil fuels.[1–5] The oxygen evolution reaction (OER) is the most fundamental process involved in a series of energy conversion devices (*e.g.*, water electrolyzers, metal–air batteries, and regenerative fuel cells). However, its four proton–electron-transfer multistep process accompanied by oxygen–oxygen bond formation causes a sluggish reaction kinetics with a large overpotential.[6] To increase the catalytic efficiency, a number of earth-abundant-metal-based electrocatalysts have been developed, such as oxides, chalcogenides, and pnictides. Some of them show superior OER performance, even surpassing the benchmark Ir- or Ru-based oxides, but their catalytic activity is still limited by the scaling relations for the variable energies of different adsorbed intermediates.[7–11] Therefore, it is highly desirable to identify the structure of the catalytically active sites on the catalysts' surface and unveil the OER mechanisms under the dynamic reaction conditions, offering guidelines for the rational and targeted designs of electrocatalysts.

Recently, a batch of studies have demonstrated that automatic structural reconstruction occurred on the surface of the as-prepared OER electrocatalysts during the anodic oxidation process, as a result, making them be irreversibly converted to the oxy- or hydroxides,[10,12–17] In this regard, these electrocatalysts under non-reaction conditions should be called ''precatalysts'' rather than the ''true catalyst''. One more interesting finding is that, in most cases, the reconstructed active oxy/hydroxides display better OER performances than those of the as-synthesized bulk counterparts *via* other direct chemical routes. This phenomenon is also widely observed in metal sulfide electrocatalysts, which have versatile electronic structures and atomic arrangements as promising candidates to replace novel metal oxides.[6,7,14] However, it remains greatly difficult to give a deeper insight into the underlying mechanism, owing to the complexity of the reconstructed structure. For instance, the precatalyst is generally prone to undergo surface structural reconstruction, giving rise to the typical ''core–shell'' structure, but several studies have declared that the transformation is a time-dependent process and that the oxygen species are homogeneously distributed across the resulting electrocatalysts.[18] Furthermore, *in situ* or *operando* techniques are not widely applied to track the local structural evolution around catalytically active sites, leading to a poor understanding of the fundamental origin and main determinant of the structural reconstruction. Finally, it should be pointed out that extensive research has been devoted to capturing the detailed structure and intermediate information of OER catalysts under alkaline conditions but ignored the component and structural evolution in other conditions, which hinders the establishment of the structural features of precatalysts, electro-driven reconstruction, and the true catalytically-active sites relationship with a full scenario.

In the present work, Co_9S_8-SWCNT was synthesized to investigate the structural self-optimization for generating the true catalysts in neutral and alkaline electrolytes. Noteworthy, the reconstructed catalysts displayed excellent OER performances in different electrolytes, overwhelming most of the reported non-precious metal-based catalysts. *Operando* XAFS and photoelectron spectroscopic measurements revealed that the Co_9S_8-SWCNT underwent a chameleon-like structural reconstruction under neutral/alkaline conditions, where the cobalt oxyhydroxide containing sulfur (S-CoOOH-SWCNT) was formed under alkaline conditions and it was inversely transformed into the oxygenated cobalt sulfide (O-CoS-SWCNT) under neutral conditions. Undoubtedly, such an anomalous chameleon-like structural reconstruction demonstrated by *operando* studies will stimulate more research to get a comprehensive understanding under different operating conditions. Further, it sheds light on the very essence of the structural self-optimization process of OER catalysts and provides an in-depth insight into the catalytic mechanism for guiding the rational design of advanced OER electrocatalysts.

Results and discussion

Structural characterizations of the as-prepared Co_9S_8-SWCNT

The Co_9S_8-SWCNT was synthesized *via* a solvothermal route, where Co_9S_8 nanopatches were *in situ* grown on SWCNT (more details in the Experimental section). The structural information of Co_9S_8-SWCNT was identified by a series of advanced characterizations. As shown in Fig. 1a, the X-ray diffraction (XRD) pattern corresponds well with the standard Co_9S_8 phase (Joint Committee on Powder Diffraction Standards (JCPDS) No. 65-6801). The characteristic peak located at 652 cm^{-1} (A_1 mode) in the Raman spectroscopy further validated the above XRD result (Fig. S1, ESI†).[19,20] The morphology of the Co_9S_8-SWCNT was observed by transmission electron microscopy (TEM, Fig. S2, ESI†) and scanning electron microscopy (SEM, Fig. 1b). These confirmed the complete Co_9S_8 nanosheets were systematically affixed to the SWCNT' surface and thus formed a relatively regular hybrid structure. The high-resolution TEM (HRTEM, Fig. 1c) image presented two clear lattice fringes with spacing values of 0.248 and 0.286 nm with a crystal plane angle value of 55°, which could be assigned to the (400) and (222) crystal planes of Co_9S_8. Moreover, the corresponding FFT image was consistent with the HRTEM observations (inset in Fig. 1c). The elemental mapping images (Fig. 1g) when viewed at a large scale show a homogeneous distribution of Co, S, and C elements in the Co_9S_8-SWCNT. Moreover, the surface composition of Co_9S_8-SWCNT was investigated by highly sensitive synchrotron radiation photoelectron spectroscopy (SRPES, Fig. S3–S5, ESI†) which has the advantages of a large luminous flux and high ionization cross-section. In the high-resolution spectra of Co 2p, the pair of peaks at 778.9 and 793.9 eV belonged to Co–S,[21,22] while another pair of strong peaks located at 781.7 and 797.5 eV could be assigned to Co–O,[22,23] which were mainly derived from the surface oxidation. Besides, a pair of characteristic peaks at

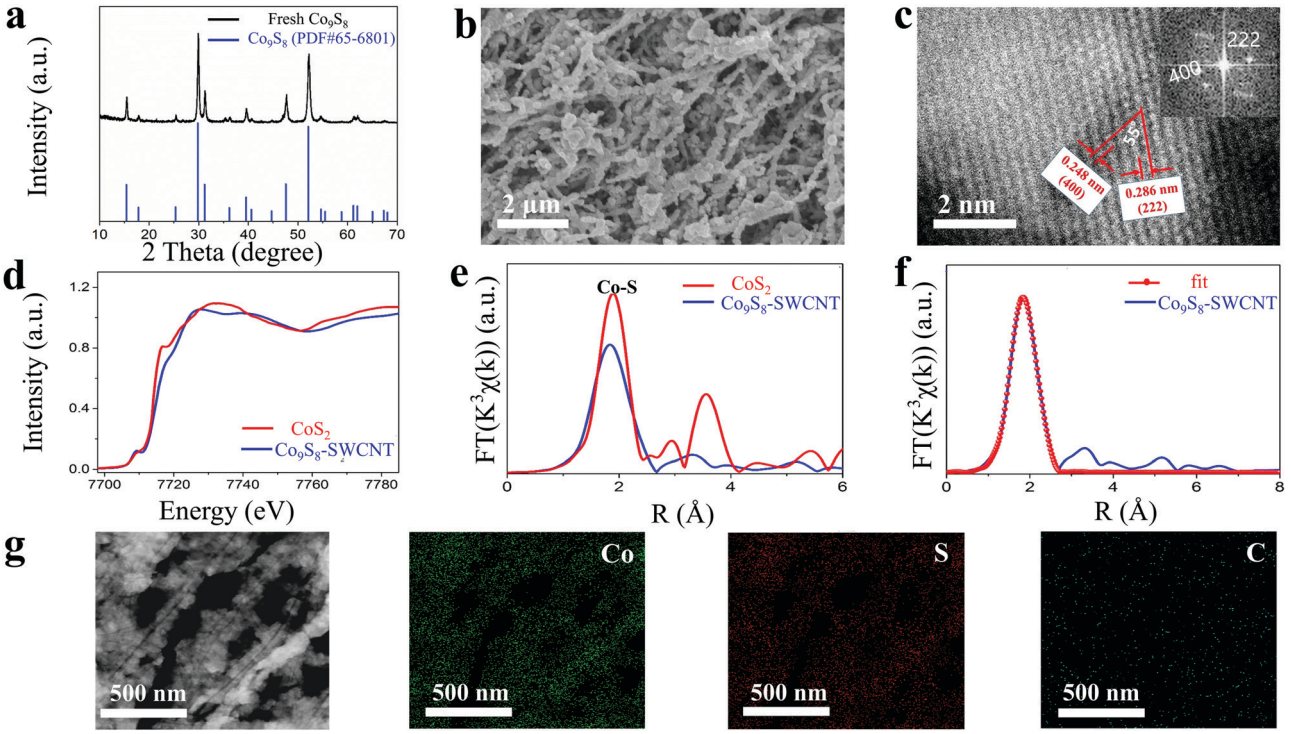

Fig. 1 Morphological and structural characterizations of Co_9S_8-SWCNT. (a) XRD of Co_9S_8 powder. (b) SEM of Co_9S_8-SWCNT. (c) HRTEM of Co_9S_8-SWCNT. (d) Co K-edge XANES spectra of Co_9S_8-SWCNT with the commercial CoS_2 reference. (e) The corresponding FT-EXAFS spectra. (f) The XAFS fitting result of Co_9S_8-SWCNT at R space. (g) HAADF-STEM element mapping images of Co_9S_8-SWCNT.

162.0 and 163.2 eV in the S 2p XPS spectra further validated the above analysis.[23,24]

Alternatively, Co_9S_8-SWCNT was characterized by synchrotron-based X-ray absorption near-edge structure (XANES) spectroscopy, which is sensitive to the partial electronic and geometric structures of related materials. The Co K-edge XANES spectrum of Co_9S_8-SWCNT (Fig. 1d) was similar to that of CoS_2, illustrating that Co_9S_8-SWCNT shared an analogous structure with cobalt disulfide. Extended X-ray absorption fine structure (EXAFS) was employed to capture detailed information about the coordination structures. Fig. 1e depicts the Fourier-transformed (FT) spectra of the extended XAFS (FT-EXAFS) curves of Co_9S_8-SWCNT. The only peak located at 1.85 Å matched the reference CoS_2 and corresponded to Co–S bonds. Moreover, the fitting result gave the precise structural information, which was in agreement with the Co_9S_8 structure (Fig. 1f and Table S1, ESI†). Furthermore, C K-edge XANES results were collected to unravel the strong interaction between SWCNT and Co_9S_8 nanosheets. There were three peaks (labeled C_1, C_2, and C_3) in the spectra (Fig. S6, ESI†), with C_1 and C_3 attributed to C 1s π^* and 1s σ^* states, respectively, while C_2 was derived from the C–S bonds,[25,26] illustrating that Co_9S_8 *in situ* sprouted on the surface of SWCNT with an intimate interface. There was more evidence from the Co L-edge spectra. Compared to Co_9S_8 powder, the Co L-edge XANES spectrum of Co_9S_8-SWCNT was shifted toward the low energy direction, suggesting electrons transfer from SWCNT to Co_9S_8 nanosheets (Fig. S7, ESI†). This could be confirmed by the normalized XANES spectra of the Co K-edge for both samples as well (Fig. S8, ESI†). This strong interfacial structure ensures a fast electron transfer from the catalyst to active sites, thus facilitating the catalytic process over the as-prepared sample.[11,27] Upon acquiring information about the structural signature and electronic states of Co_9S_8-SWCNT, we evaluated its catalytic performance, tracked the structural self-optimization, and identified the true catalysts during the OER process.

Catalytic activity for OER

To evaluate the catalytic performance of Co_9S_8-SWCNT, we conducted the measurements for the electrochemical OER in alkaline (1 M KOH)/neutral (1 M phosphate buffer solution, PBS) conditions, respectively (see the Experimental section).

As shown in Fig. 2a, the Co_9S_8-SWCNT exhibited excellent OER activity under alkaline conditions, shown by the overpotentials of 150 mV and 370 mV at current densities of 10 mA cm^{-2} and 100 mA cm^{-2} (based on the geometric area of the modified electrodes), respectively, which were lower than those of CoOOH-SWCNT, Co_9S_8 powder, and pure SWCNT. The OER Tafel slopes of the samples were investigated through the corresponding polarization curves.[28] As shown in Fig. 2b, the value of Co_9S_8-SWCNT was only 54 mV dec^{-1}, which was smaller than those of IrO_2 (63 mV dec^{-1}) and CoOOH-SWCNT (127 mV dec^{-1}). This implied a more favorable reaction kinetics and the advantageous industrial application potential for Co_9S_8-SWCNT.[29,30] Considering the unique morphology of Co_9S_8-SWCNT, it is reasonable to infer that its large electrochemical

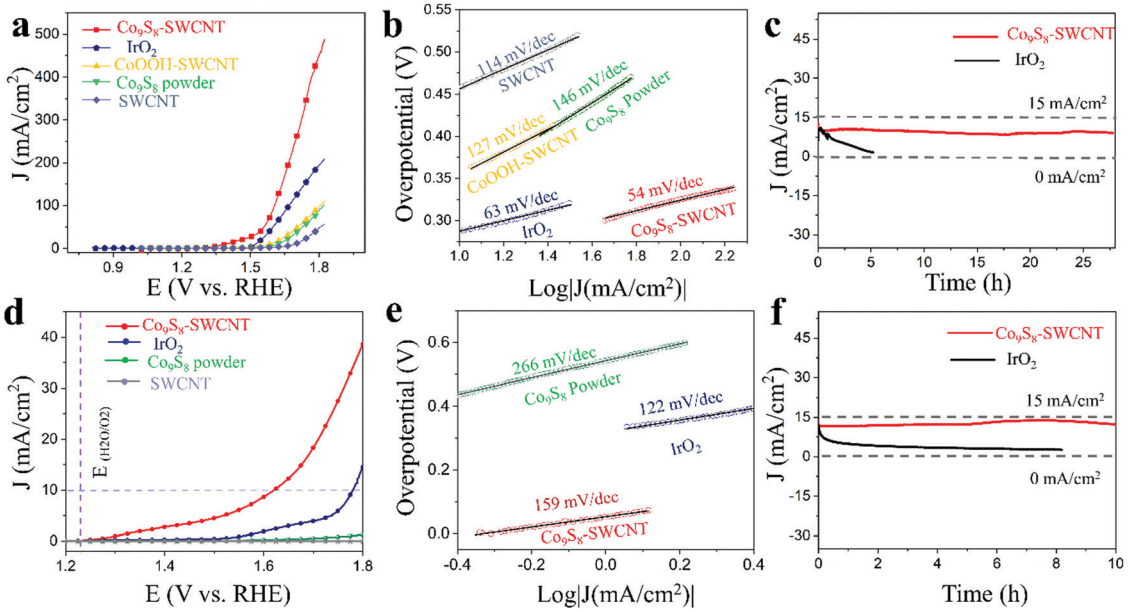

Fig. 2 Electrocatalytic OER performance of Co_9S_8-SWCNT under alkaline/neutral electrolytes. (a–c) LSV curves, Tafel plots, and the chronoamperometry (*i*–*t*) curves of Co_9S_8-SWCNT and other reference samples in 1 M KOH. (d–f) LSV curves, Tafel plots, and the chronoamperometry (*i*–*t*) curves of Co_9S_8-SWCNT and other reference samples in 1 M PBS.

active surface area (ECSA) contributes to its high catalytic activity. Cyclic voltammetry (CV) was employed to measure the double-layer capacitance (C_{dl}), and then the ECSA was deduced according to the proportional relationship between them (Fig. S9, ESI†). The C_{dl} of Co_9S_8-SWCNT was up to 7.88 mF, which was nearly 2.5 times that of the CoOOH-SWCNT and 11 times that of the Co_9S_8 powders, respectively. Moreover, it is worth noting that the catalytic performance of Co_9S_8-SWCNT was far superior to that of the reference catalysts, implying that Co_9S_8-SWCNT possessed a higher intrinsic activity apart from the larger ECSA too. To rule out the effect of external factors (surface area, loading, *etc.*), the classic specific activity was used to reveal the intrinsic activities of the catalysts.[31,32] At an overpotential of 350 mV (based on previously reported device models that indicated a 10% efficient solar water-splitting device should be $\eta < 0.45$ V, assuming that reasonable HER catalysts works at $|\eta| \sim 0.1$ V, thus leaving a $\sim$0.35 V overpotential available for OER). The specific current density $J_{s,\eta=0.35\,V}$ of Co_9S_8-SWCNT was 0.043 mA cm^{-2}, which was 3.3 times that of CoOOH-SWCNT (0.013 mA cm^{-2}) and 1.4 times that of Co_9S_8 powder (0.031 mA cm^{-2}). Notably, the electronic/chemical coupling effect between SWCNT and Co_9S_8 nanosheets can explain why Co_9S_8-SWCNT exhibited a better intrinsic activity than Co_9S_8 powder (Fig. S6–S8, ESI†). However, the Co_9S_8 powder showed higher activity than CoOOH-SWCNT, suggesting the structural self-optimization may induce an enhanced intrinsic activity. In addition, as another important parameter reflecting the intrinsic activity, the turnover frequency (TOF) values of the samples were also calculated. We drew a TOF map (Fig. S10, ESI†) based on a rough assumption that all the metal atoms of Co_9S_8-SWCNT are electrochemically active sites (Table S2, ESI†). Such high TOF values imply a superior intrinsic activity of Co_9S_8-SWCNT. Moreover, the stability is another key figure of merit for desirable electrocatalysts. The chronoamperometry curve of Co_9S_8-SWCNT in Fig. 2c showed that there was no observable degradation during the continuous operation (almost 30 h). The electrochemical impedance spectroscopy (EIS) of Co_9S_8-SWCNT showed a smaller semicircle than the other reference catalysts (Fig. S11, ESI†), implying a low charge transfer resistance (R_{ct}) from the bulk electrolyte to the electrode surface with a fast OER kinetics for Co_9S_8-SWCNT.

Furthermore, a successive OER (disk electrode)–ORR (ring electrode) process was carried out to verify that the observed current was derived from OER and then the faradaic efficiency was estimated (Fig. S12, ESI†). Oxygen was generated at a disk current of 120 μA, which was further reduced by sweeping across the Pt ring electrode at 0.5 V (ORR potentials). The corresponding current from the Pt ring electrode was 44 μA, and thus the faradaic efficiency of Co_9S_8-SWCNT was determined to be 99.1%. The gas chromatography measurement further confirmed the observed current exclusively originated from the OER process. The detected O_2 amount fitted well with theoretical calculation, yielding a nearly 100% faradaic efficiency (Fig. S13, ESI†).

As expected, the Co_9S_8-SWCNT also exhibited superb OER activity with a more negative applied potential of 1.60 V (*vs.* RHE) to deliver a current density of 10 mA cm^{-2} in 1 M PBS (Fig. 2d). Similarly, the values of TOF and ECSA for Co_9S_8-SWCNT were higher than those of the reference catalysts (Fig. S14 and S15, ESI†) under neutral conditions, suggesting a higher intrinsic activity and more exposed active sites. The Tafel slope of Co_9S_8-SWCNT was 159 mV dec^{-1}, comparable to commercial IrO_2 (122 mV dec^{-1}). A smaller Tafel slope implies a lower energy consumption in electrochemical

processes (Fig. 2e).[29] The chronoamperometry curve (Fig. 2f) showed no obvious degradation over 10 h at a constant potential of 1.6 V (*vs.* RHE). In addition, a small R_{ct} gives it faster OER kinetics under neutral conditions (Fig. S16, ESI†). Finally, the faradaic efficiency of Co_9S_8-SWCNT toward neutral OER was determined to be 97.3% (Fig. S17, ESI†) through the successive OER (disk electrode)–ORR (ring electrode) process.

Co_9S_8-SWCNT after OER at pH 14 (CSST-14)

Based on previous reports,[6,8,33,34] how the structure of the catalyst changes as a result of the self-reconstruction during the OER process is still poorly understood. From the CV curves as shown in Fig. 3a, it can be seen an *in situ* electrochemical tuning process occurred for Co_9S_8-SWCNT. A broad and obvious oxidation peak located at *ca.*1.3 V (*vs.* RHE) appeared only in the first CV scan, and then it disappeared completely in subsequent CV scans. This could infer that the Co_9S_8-SWCNT experienced an irreversible self-optimization during the OER process under alkaline conditions.[35–39] XRD analyses suggested that the major phase of CSST-14 was β-CoOOH without the S-related phase (Fig. S18, ESI†), which could be further supported by the fact that there was S but no Co element in the electrolyte after OER as shown *via* inductively coupled plasma atomic emission spectrometry (ICP-AES, Table S3, ESI†). Furthermore, as a powerful technique that is sensitive to changes in the composition or structure, Raman spectroscopy was applied to probe the CSST-14 sample (Fig. S19, ESI†). The peaks located at 1348 and 1588 cm^{-1} could be assigned to the D-band and G-band of SWCNT.[25] A prominent G peak means a higher degree of graphitization, which provides for excellent conductivity; thereby contributing to the catalysts excellent performance,[40] which was in good agreement with the experimental results. Furthermore, when magnifying the spectrum in the range of 300 to 750 cm^{-1}, four distinct peaks appeared at 466, 518, 605, and 670 cm^{-1} that could be ascribed to CoOOH.[41,42] Besides, the SEM/TEM images (Fig. S20, ESI†) indicated that the original Co_9S_8-SWCNT had self-reconstructed into a film covered on SWCNT. HRTEM was also employed to examine the morphology of CSST-14. As represented in Fig. 3b, CSST-14 exhibited two continuous lattice fringes with lattice spacings of 1.96 Å and 1.80 Å, respectively, and a crystal plane angle of 135°, which correlated with the (221) and (211) planes of β-CoOOH (JCPDS No. 72-2280). Notably, it also presents numerous amorphous regions after OER, which was consistent with the XRD pattern. This highly disordered structure may guarantee the superior electrocatalytic activity of CSST-14.[23,43] The elemental mapping of CSST-14 indicated a homogeneous distribution of Co, O, and C elements in the entire sample (Fig. S21, ESI†). Surprisingly, a few S elements were still evenly distributed on the CSST-14, which has been overlooked in previous reports.[39,44] The synchrotron-based quasi-*in situ* Fourier transform-infrared (FT-IR) spectrum also revealed that Co–O bonds appeared after OER while Co–S bonds remained (Fig. S22, ESI†).[45,46] Additionally, XPS data were further collected to explore the composition and reveal the chemical state of CSST-14. In the high-resolution Co 2p XPS spectra (Fig. S23, ESI†), a pair of peaks located at 780.5 and 795.6 eV could be assigned to β-CoOOH.[8,33,47,48] Also, the S 2p XPS spectra further confirmed the S elements in CSST-14 (Fig. S24, ESI†). From the Co L-edge XANES, CSST-14 showed the same features as β-CoOOH except that it was shifted slightly to the low energy direction, which further suggested that CSST-14 was S-CoOOH (Fig. 3c).[49]

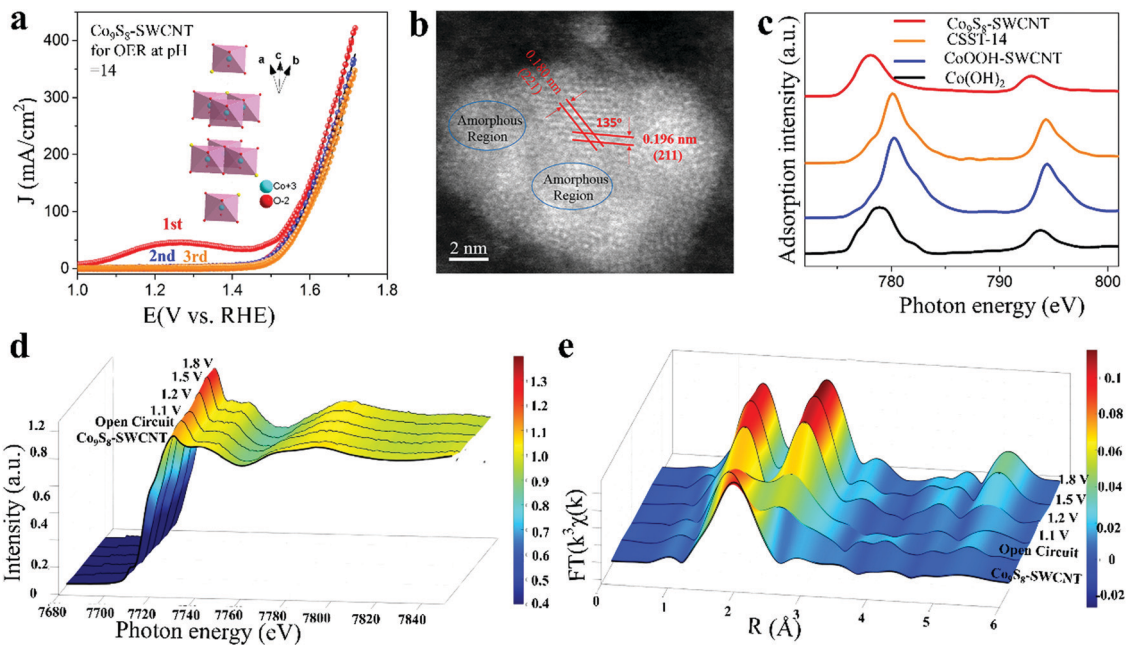

Fig. 3 Co_9S_8-SWCNT for the alkaline OER. (a) The first three CV curves of Co_9S_8-SWCNT. (b) HRTEM of Co_9S_8-SWCNT after the OER at pH 14. (c) Co L-edge XANES spectra of Co_9S_8-SWCNT after the OER at pH 14. (d and e) *Operando* XAFS visualizing structural self-optimization on Co_9S_8-SWCNT during the alkaline OER process.

Although β-CoOOH was the body of the true catalyst, the effect of the residual S element on the catalytic performance cannot be ignored. Inspired by a previous report, CSST-14 was immersed in a 0.1 mM Zn^{2+} solution to block the surface S sites.[50] As predicted, the catalytic activity decreased with increasing the immersion time, and almost all the S sites were locked after 60 s (Fig. S25, ESI†). In sharp contrast, the catalytic performance of CSST-14 showed only a negligible change even after 120 s in H_2O. The aforementioned results strongly confirm that the surface S sites are critical for a high catalytic activity.[50–53] Based on the previous reports, the S in the catalyst may tune the electrochemical performance by the following: (1) by improving the conductivity of the catalysts, which is significant to the enhanced catalytic performance;[54] (2) by enhancing the catalytic stability and performance by stabilizing the high valence state of active metals, which are often catalytically active sites;[55] (3) by directly participating in the reaction by adjusting the adsorption intermediate state;[56,57] (4) by accelerating the proton charge-transfer process as proton acceptors, and by enhancing the hydrophilicity of CSST-14.[58,59]

Co_9S_8-SWCNT after OER at pH 7 (CSST-7)

A similar irreversible self-optimization process was also observed under neutral conditions (Fig. 4a).[35–39] XRD showed that the main diffraction peaks matched well with that of CoS but were shift to the high direction, which might have been induced by heteroatom doping (Fig. S26, ESI†).[40,60] The TEM and SEM images indicated a distinct change of Co_9S_8-SWCNT after the OER (CSST-7), where the previously regular structure was transformed into a film wrapped on the SWCNT (Fig. S27, ESI†). Such a drastic structural reconstruction has also been observed recently.[8,39,61] The HAADF-STEM images at sub-atomic resolution (Fig. 4b) revealed that the cobalt atoms were distributed in a hexagonal array pattern, in which the nearest distance between two atoms was 3.36 Å, which was well consistent with that of the (001) crystal face of the CoS. All the elements (Co, S, O, and C) were evenly distributed throughout the CSST-7 according to the elemental mapping (Fig. S28, ESI†). It is worth noting that oxygen element in CSST-7 was significantly increased when compared with Co_9S_8-SWCNT. Furthermore, the ICP-AES tests showed that a minimal amount of Co and no S elements could be detected in the electrolyte after the OER (Table S4, ESI†). Structural self-optimization inevitably leads to changes in the surface chemical states. In the high-resolution XPS spectra of Co 2p (Fig. S29, ESI†), Co 2p was shifted to a high energy direction by 0.7 eV after the OER when compared with the pristine Co_9S_8-SWCNT, indicating a higher oxidation state of Co species in CSST-7.[19,62] The Co L-edge XANES spectra further validated this conclusion (Fig. 4c), where the Co $L_{2,3}$-edges of the CSST-7 showed a similar shape to that of the original except for a shift toward a higher energy direction. Based on the above results, it is safe to conclude that the main component of CSST-7 was oxygenated CoS-SWCNT (O-CoS-SWCNT).

Self-optimization mechanism and tracking the source of the high catalytic activity

The importance of understanding the nature of self-optimization and capturing the reaction pathway are undeniable.[6] Fortunately, advanced *operando* XAFS makes it possible to visualize the self-optimization process under working conditions. From the Co K-edge XANES spectra (Fig. 3d), the self-optimization of Co_9S_8-SWCNT started at an open circuit voltage and then

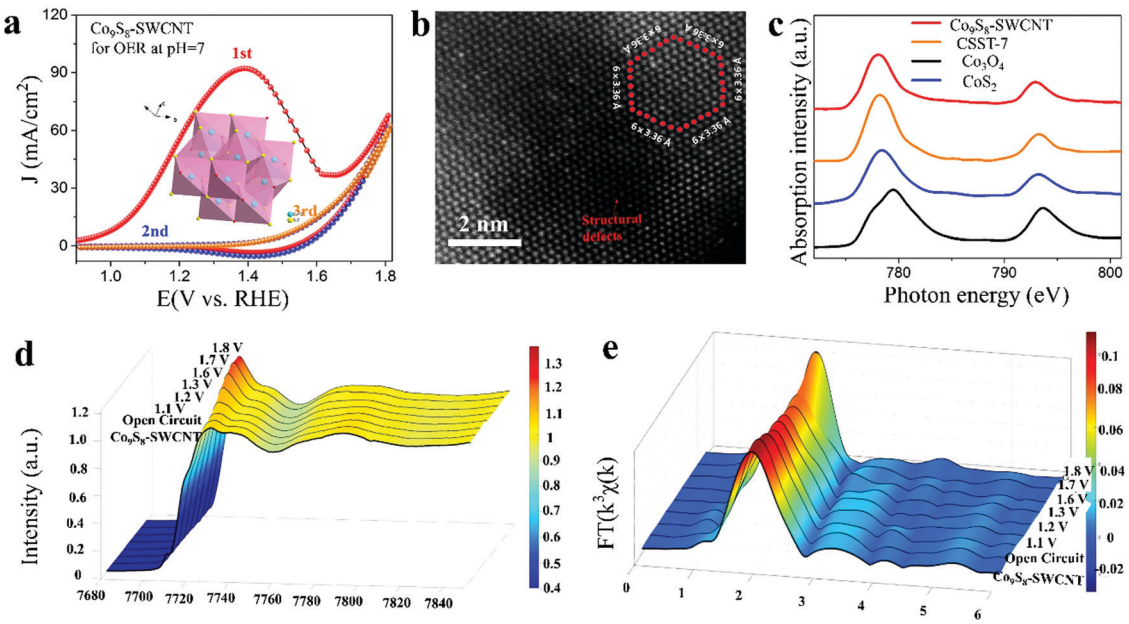

Fig. 4 Co_9S_8-SWCNT for the neutral OER. (a) The first three CV curves of Co_9S_8-SWCNT. (b) HRTEM of Co_9S_8-SWCNT after OER at pH 7. (c) Co L-edge XANES spectra of Co_9S_8-SWCNT after the OER at pH 7. (d and e) *Operando* XAFS visualizing the structural self-optimization of Co_9S_8-SWCNT during the neutral OER process.

gradually transformed into S-CoOOH-SWCNT when the voltage was stepped up to 1.2 V. The absorption edge energy of Co_9S_8-SWCNT moved toward a high-energy direction with the increasing voltage and finally reached a steady state. Subsequently, Fourier-transformed Co K-edge EXAFS spectra and the corresponding quantitative fitting results (Fig. 3e and Table S5, ESI†) were utilized to depict the process intuitively. This can be described as follows. With the increase in the applied potentials, Co–O and Co–Co bonds begin to appear along with the fading of Co–S bonds, and finally S-CoOOH-SWCNT is formed, as also evidenced by the aforementioned results.

Similarly, *operando* XAFS was also used to visualize the structural self-optimization of the catalyst during the OER under neutral conditions, where the self-optimization process starts after the voltage of 1.1 V. As the voltage rises, the Co_9S_8-SWCNT is gradually oxidized until the voltage reaches 1.6 V and it achieves a steady state, which is considered as a true catalyst (Fig. 4d and e).

The behavior of Co_9S_8-SWCNT self-optimizing into S-CoOOH-SWCNT or O-CoS-SWCNT depending on the actual working environment is similar to a chameleon. In particular, precatalysts will self-optimize into a favorable phase under the actual conditions (pH, voltage, *etc.*), which is exactly the case for a true catalyst. To validate this hypothesis, we performed additional OER tests in buffer solutions of pH 5 (acetic acid–sodium acetate buffer solution) and pH 10 (ammonia–ammonium chloride buffer solution), and found that Co_9S_8-SWCNT also showed excellent catalytic performances under these conditions (Fig. S30 and S31, ESI†). Furthermore, XAFS suggests that CSST-5 remains a phase of Co_9S_8, but CSST-10 transforms into O-CoS (Fig. S32–S35, ESI†). At present, we can draw the conclusion that the structural self-optimization plays a crucial role in reconstructing the precatalyst into the truly active catalyst, which is a beneficial stable phase under the actual conditions.

Conclusions

We elaborately designed a highly efficient OER catalyst for both alkaline and neutral conditions. Structural self-optimization endowed the prepared catalyst with superb catalytic activity. Considering the irreversible behavior of CV cycles, we visualized the structural self-optimization of C_9S_8-SWCNT under neutral/alkaline conditions *via operando* XAFS and other advanced characterizations. We accidentally found that Co_9S_8-SWCNT underwent a disproportionate self-reconstruction under different conditions. The precatalyst of Co_9S_8-SWCNT self-optimized into S-CoOOH-SWCNT as a true catalyst for the OER under alkaline condition, whereas it transformed into O-CoS-SWCNT under neutral conditions. Combining the experimental results of CSST-5 and CSST-10, it was confirmed that the self-optimization in the precatalyst displays a chameleon-like behavior, that is, it will transform into its most favorable phase based on the actual working conditions and will then work as a true catalyst. Our study will hopefully stimulate more researchers to study the OER under different conditions toward gaining a more comprehensive understanding. More importantly, this work sheds light on the nature of the structural self-optimization process and provides an in-depth insight into the catalytic mechanism, and thus we strongly believe that it will provide new ideas for the fields of chemistry and catalysis.

Experimental

Synthesis of the catalysts

The thioacetamide (TAA), commercial IrO_2, and *N*,*N*-dimethylformamide (DMF) were purchased from Aladdin Chemistry Co. Ltd, while the cobaltous chloride ($CoCl_2{\cdot}6H_2O$) was from Sinopharm Chemical Reagent Co. Ltd. All the chemicals were directly used without further purification. We prepared Co_9S_8-SWCNT with the solvothermal method. The reference sample of β-CoOOH-SWCNT was prepared according to a previous report, except for adding purified SWCNT,[63] and was then characterized by XRD (Fig. S36, ESI†).

At first, the preparation and purification of single-wall carbon nanotubes (SWCNTs) were exactly the same as in our previous works.[30,64] Here, 2 mmol $CoCl_2{\cdot}6H_2O$ and 10.1 mmol of TAA were dissolved in 30 mL DMF and stirred well, and then the purified SWCNT films were immersed in the solution for several hours. Finally, the solution was transferred to a 40 mL Teflon-lined stainless steel autoclave and the temperature was set at 200 °Cfor 24 h. The Co_9S_8-SWCNT was collected after it had cooled down to room temperature and was then rinsed with ethanol and water three times respectively. We made a preliminary judgment that the Co_9S_8 nanosheets had been *in situ* grown on SWCNT if the color of the complex changed from black to silver white. It should be noted that we obtained Co_9S_8 powder by centrifuging the above solution when the Co_9S_8-SWCNT film had been removed. These freestanding precatalyst films were immersed in ethanol for further characterization and measurement, while the Co_9S_8 powder was placed in a sealed container after it had been dried.

Electrochemistry

All the electrochemical measurements were carried out on an electrochemical work station (CHI 760e, China) in a standard three-electrode setup with graphite rods and Ag/AgCl (saturated KCl solution) or Hg/HgO (1 M KOH) electrode as the counter and reference electrodes, respectively. Typically, the glassy carbon working electrode was modified as following two different methods: the freestanding catalyst film was cut into a shape and size similar to the glassy carbon electrode (3 mm diameter), and then loaded onto the glassy carbon electrode surface. Finally, a drop of 5 wt% Nafion solution was dropped onto the surface of the composites to protect it from shedding.[25,30] As for Co_9S_8 powder, we prepared them completely differently, whereby 4 mg Co_9S_8 powders were dispersed in a mixture solution of H_2O (0.5 mL), ethanol (0.46 mL), and 5% Nafion solution (0.04 mL) by sonication for at least 30 min. Finally, 5 μL of the ink was drop-cast onto the glassy carbon working electrode and left to dry overnight.

All the electrochemical tests were performed in 1 M KOH solution or 1 M PBS, and all the applied potentials had been converted with respect to the reversible hydrogen electrode (RHE) by the following calculations: $E_{RHE} = E_{Ag/AgCl} + 0.197\ V + 0.059 \times pH$ or $E_{RHE} = E_{Hg/HgO} + 0.098\ V + 0.059 \times pH$. Prior to the linear sweep voltammogram (LSV) tests, the catalysts were activated by CV, and then the LSV was recorded from 1.0 to 1.8 V (*vs.* RHE) at a scan rate of 5 mV s^{-1} with 85% IR compensation. We obtained the Tafel slope by plotting the overpotential η against log (current density, J). The CV curves were measured with scan rates of 0.01, 0.02, 0.03, 0.04, 0.05, and 0.06 V s^{-1} at the potential window from 0.20 to 0.35 V (*vs.* Hg/HgO) for the alkaline electrolyte or from 0.3 to 0.5 V (*vs.* Ag/AgCl) for the neutral electrolyte to estimate the double-layer capacitances C_{dl}.

$$C_{dl} = \frac{i_c}{\nu}$$

where all the current is assumed to be due to capacitive charging and i_c is the double-layer charging current and ν is the scan rate.

ECSA could be obtained according to the relationship between C_{dl} and ECSA by:

$$ECSA = \frac{C_{dl}}{C_s}$$

where C_s is the specific capacitance of the sample or the capacitance of an atomically smooth planar surface of the material per unit area under identical electrolyte conditions. Here, we used the general value of 60 μF cm^{-2} in this work.[12,65]

To exclude the external factors (surface area, loading, *etc.*) interference in the electrochemical performance evaluation, the specific current density per catalyst surface area (j_s) of samples was calculated.[32,66]

$$R_f = \frac{ECSA}{A(\text{geometric area})}$$

$$J_s = \frac{J_g}{R_f}$$

where R_f is the roughness factor, A represent the geometric area of the catalysts, and J_g is the apparent current density based on the geometric area of the catalysts.

As durability is one of most important criteria for satisfactory electrocatalysts, we performed chronoamperometry to test the durability of our samples. Electrochemical impedance spectra were measured at frequencies ranging from 100 kHz to 0.01 Hz at an overpotential of 300 mV (alkaline conditions) and 450 mV (neutral conditions), respectively, and at an AC voltage of 5 mV.

The turnover frequency (TOF) was calculated based on the following equation:

$$TOF = \frac{J \times A}{4 \times F \times n}$$

where J is the current density at a given overpotential, A is the geometric surface area of the Co_9S_8-SWCNT, 4 means there are 4 electrons participating in electrochemical processes for OER, F is the Faraday constant (96485.3 C mol^{-1}), and n is the mole number of active sites on the modified electrode.

The Co_9S_8-SWCNT was monitored with a rotating ring disk electrode (RRDE) in N_2-saturated 1 M KOH to test faradaic efficiency. We conducted RRDE measurements in 1 M KOH at a scan rate at 5 mV s^{-1} under a generic rotational rate of 1600 rpm. The oxygen produced (OER) by the disk electrode was then reduced (ORR) at the surrounding Pt ring electrode at a fixed potential of 0.5 V. The faradaic efficiency (FE) was calculated by using the following formula: $FE = I_r/(I_d \times N)$, where I_r is the ring-current, I_d is the disk-current, and N is the collection efficiency of the RRDE (this work, N = 0.37). Furthermore, we directly measured the gas produced during the OER process through a gas chromatograph (GC, 7890B).

XAFS

The s-XAS were collected by total electron yield (TEY) mode at the beam-line XMCD at the National Synchrotron Radiation Laboratory (NSRL) with the photon energy resolution of 0.2 eV. *Ex situ* and *operando* XAFS measurements were performed at the beamline 1W1B at the Beijing Synchrotron Radiation Facility (BSRF). All the X-ray was monochromatized by a double-crystal Si(111) monochromator for BSRF. It should be pointed out that the *ex-situ* XAFS were measured in transmission mode, while *operando* XAFS was performed in fluorescence mode. The energy of the Co K-edge was calibrated by a cobalt metal foil. Owing to our samples being free-standing, we put the Co_9S_8-SWCNT into the *in situ* cell as the working electrode to do the *operando* XAFS experiments in alkaline and neutral conditions. The acquired XAS data were processed and analyzed by using the WinXAS 3.1 program following the standard procedures.[67] The theoretical amplitudes and phase-shift functions of Co–O, Co–S, and Co–Co were calculated with the FEFF8.2. code.[68]

Characterizations

Powder X-ray diffraction (XRD) was carried out on a Philips X'Pert Pro Super diffractometer equipped with Cu Kα radiation (λ = 1.54178 Å) to characterize the samples. To explore the composition and valence information of the samples on the surface, X-ray photoelectron spectroscopy (XPS) was carried out the photoemission endstation at the National Synchrotron Radiation Laboratory (NSRL). The morphology and size observations were obtained with a JEOL JSM-6700F SEM instrument. Transmission electron microscopy (TEM) and high-resolution TEM (HRTEM) measurements were taken on a JEM-2100F field emission electron microscopy system with an acceleration voltage of 200 kV for accurate structural information. The high-angle annular dark-field scanning transmission electron microscopy images (HAADF-STEM) were obtained on a Talos F200X atomic resolution analytical microscope (200 kV). We obtained the Co K-edge XAFS spectra of the samples from the Beijing Synchrotron Radiation Facility (1W1B, BSRF), while s-XAS was performed at NSRL. The content and species of the elements were explored with an Optima 7300DV inductively coupled plasma-atomic emission spectrometry (ICP-AES)

system. Raman spectra were obtained through a Horiba XploRA Raman system with a 532 nm Ar laser. Gas chromatography was performed on an Agilent 7890B system equipped with a quantitative loop. Fourier transform-infrared (FT-IR) spectra of the samples were recorded by infrared spectroscopy and microspectroscopy endstation NSRL.

Author contributions

L. S. supervised the project. D. F. C., D. B. L. and S. M. C. designed the work and carried out most of the experiments. O. A. M. helped to prepare most of the samples. W. J. X. and C. D. W. performed XAFS and s-XAS experiments. S. Q. C., L. R. Z. and J. Z. guided the *operando* XAS measurements and helped to analyze XAS results. C. Q. W. and B. H. G. helped to character the samples with TEM. H. L. J. revised the manuscript and gave helpful discussions. X. J. C. and X. J. W. helped to explain some experimental date. All the authors discussed the results and assisted during the manuscript preparation.

Conflicts of interest

The authors declare no competing interests.

Acknowledgements

This work was financially supported in part by National Key R&D Program of China (2017YFA0303500), NSFC (U1932201, 11574280, 21727801 and 51902303), NSFC-MAECI (51861135202), CAS Key Research Program of Frontier Sciences (QYZDB-SSW-SLH018), CAS International Partnership Program (211134-KYSB20190063) and CAS Collaborative Innovation Program of Hefei Science Center (2019HSC-CIP002) and CAS Iterdisciplinary Innovation Team. L. S. acknowledges the support from Key Laboratory of Advanced Energy Materials Chemistry (Ministry of Education), Nankai University (111 project, B12015). We thank the Beijing Synchrotron Radiation Facility (1W1B and Soft-X-ray endstation, BSRF), the Hefei Synchrotron Radiation Facility (Infrared Spectroscopy and Microspectroscopy, ARPES, MCD-A and MCD-B Soochow Beamline for Energy Materials, Photoemission and Catalysis/Surface Science Endstations at NSRL), and the USTC Center for Micro and Nanoscale Research and Fabrication for helps in characterizations.

Notes and references

1 X. Zou, Y. Wu, Y. Liu, D. Liu, W. Li, L. Gu, H. Liu, P. Wang, L. Sun and Y. Zhang, *Chem*, 2018, **4**, 1139–1152.
2 I. Roger, M. A. Shipman and M. D. Symes, *Nat. Rev. Chem.*, 2017, **1**, 0003.
3 B. Zhang, X. Zheng, O. Voznyy, R. Comin, M. Bajdich, M. Garcia-Melchor, L. Han, J. Xu, M. Liu, L. Zheng, F. P. Garcia de Arquer, C. T. Dinh, F. Fan, M. Yuan, E. Yassitepe, N. Chen, T. Regier, P. Liu, Y. Li, P. De Luna, A. Janmohamed, H. L. Xin, H. Yang, A. Vojvodic and E. H. Sargent, *Science*, 2016, **352**, 333–337.
4 A. Grimaud, O. Diaz-Morales, B. Han, W. T. Hong, Y. L. Lee, L. Giordano, K. A. Stoerzinger, M. T. M. Koper and Y. Shao-Horn, *Nat. Chem.*, 2017, **9**, 457–465.
5 H. Fei, J. Dong, Y. Feng, C. S. Allen, C. Wan, B. Volosskiy, M. Li, Z. Zhao, Y. Wang, H. Sun, P. An, W. Chen, Z. Guo, C. Lee, D. Chen, I. Shakir, M. Liu, T. Hu, Y. Li, A. I. Kirkland, X. Duan and Y. Huang, *Nat. Catal.*, 2018, **1**, 63–72.
6 S. Jin, *ACS Energy Lett.*, 2017, **2**, 1937–1938.
7 J. Hao, W. Yang, Z. Peng, C. Zhang, Z. Huang and W. Shi, *ACS Catal.*, 2017, **7**, 4214–4220.
8 H. Jiang, Q. He, X. Li, X. Su, Y. Zhang, S. Chen, S. Zhang, G. Zhang, J. Jiang, Y. Luo, P. M. Ajayan and L. Song, *Adv. Mater.*, 2019, **31**, 1805127.
9 L. Yu, J. F. Yang, B. Y. Guan, Y. Lu and X. W. D. Lou, *Angew. Chem., Int. Ed.*, 2018, **57**, 172–176.
10 P. Chen, K. Xu, Z. Fang, Y. Tong, J. Wu, X. Lu, X. Peng, H. Ding, C. Wu and Y. Xie, *Angew. Chem., Int. Ed.*, 2015, **54**, 14710–14714.
11 M. Favaro, J. Yang, S. Nappini, E. Magnano, F. M. Toma, E. J. Crumlin, J. Yano and I. D. Sharp, *J. Am. Chem. Soc.*, 2017, **139**, 8960–8970.
12 Q. He, H. Xie, Z. U. Rehman, C. Wang, P. Wan, H. Jiang, W. Chu and L. Song, *ACS Energy Lett.*, 2018, **3**, 861–868.
13 Y. Zhang, C. Wu, H. Jiang, Y. Lin, H. Liu, Q. He, S. Chen, T. Duan and L. Song, *Adv. Mater.*, 2018, **30**, 1707522.
14 H. Jiang, Q. He, Y. Zhang and L. Song, *Acc. Chem. Res.*, 2018, **51**, 2968–2977.
15 E. Fabbri, M. Nachtegaal, T. Binninger, X. Cheng, B. J. Kim, J. Durst, F. Bozza, T. Graule, R. Schaublin, L. Wiles, M. Pertoso, N. Danilovic, K. E. Ayers and T. J. Schmidt, *Nat. Mater.*, 2017, **16**, 925–931.
16 J. Zhou, Y. Wang, X. Su, S. Gu, R. Liu, Y. Huang, S. Yan, J. Li and S. Zhang, *Energy Environ. Sci.*, 2019, **12**, 739–746.
17 M. Kim, B. Lee, H. Ju, S. W. Lee and J. Kim, *Adv. Mater.*, 2019, **31**, 1901977.
18 W. Li, X. Gao, D. Xiong, F. Xia, J. Liu, W. G. Song, J. Xu, S. M. Thalluri, M. F. Cerqueira, X. Fu and L. Liu, *Chem. Sci.*, 2017, **8**, 2952–2958.
19 J. Yang, G. Zhu, Y. Liu, J. Xia, Z. Ji, X. Shen and S. Wu, *Adv. Funct. Mater.*, 2016, **26**, 4712–4721.
20 X. Cui, Z. Chen, Z. Wang, M. Chen, X. Guo and Z. Zhao, *ACS Appl. Energy Mater.*, 2018, **1**, 5822–5829.
21 S. Wang, B. Y. Guan, X. Wang and X. W. D. Lou, *J. Am. Chem. Soc.*, 2018, **140**, 15145–15148.
22 J. Hou, B. Zhang, Z. Li, S. Cao, Y. Sun, Y. Wu, Z. Gao and L. Sun, *ACS Catal.*, 2018, **8**, 4612–4621.
23 P. Cai, J. Huang, J. Chen and Z. Wen, *Angew. Chem., Int. Ed.*, 2017, **56**, 4858–4861.
24 L. L. Wu, Q. S. Wang, J. Li, Y. Long, Y. Liu, S. Y. Song and H. J. Zhang, *Small*, 2018, **14**, 1704035.
25 D. Liu, W. Xu, Q. Liu, Q. He, Y. A. Haleem, C. Wang, T. Xiang, C. Zou, W. Chu, J. Zhong, Z. Niu and L. Song, *Nano Res.*, 2016, **9**, 2079–2087.
26 L. Ji, M. Rao, H. Zheng, L. Zhang, Y. Li, W. Duan, J. Guo, E. J. Cairns and Y. Zhang, *J. Am. Chem. Soc.*, 2011, **133**, 18522–18525.

27 P. Ganesan, M. Prabu, J. Sanetuntikul and S. Shanmugam, *ACS Catal.*, 2015, **5**, 3625–3637.
28 Y. Liu, C. Xiao, M. Lyu, Y. Lin, W. Cai, P. Huang, W. Tong, Y. Zou and Y. Xie, *Angew. Chem., Int. Ed.*, 2015, **54**, 11231–11235.
29 S. Sun, H. Li and Z. J. Xu, *Joule*, 2018, **2**, 1024–1027.
30 D. Cao, K. Ye, O. A. Moses, W. Xu, D. Liu, P. Song, C. Wu, C. Wang, S. Ding, S. Chen, B. Ge, J. Jiang and L. Song, *ACS Nano*, 2019, **13**, 11733–11740.
31 L. Li, H. Yang, J. Miao, L. Zhang, H.-Y. Wang, Z. Zeng, W. Huang, X. Dong and B. Liu, *ACS Energy Lett.*, 2017, **2**, 294–300.
32 C. C. McCrory, S. Jung, I. M. Ferrer, S. M. Chatman, J. C. Peters and T. F. Jaramillo, *J. Am. Chem. Soc.*, 2015, **137**, 4347–4357.
33 W. Chen, H. Wang, Y. Li, Y. Liu, J. Sun, S. Lee, J. S. Lee and Y. Cui, *ACS Cent. Sci.*, 2015, **1**, 244–251.
34 C. Gu, S. Hu, X. Zheng, M. R. Gao, Y. R. Zheng, L. Shi, Q. Gao, X. Zheng, W. Chu, H. B. Yao, J. Zhu and S. H. Yu, *Angew. Chem., Int. Ed.*, 2018, **57**, 4020–4024.
35 A. Bergmann, E. Martinez-Moreno, D. Teschner, P. Chernev, M. Gliech, J. F. de Araujo, T. Reier, H. Dau and P. Strasser, *Nat. Commun.*, 2015, **6**, 8625.
36 J. Masa, P. Weide, D. Peeters, I. Sinev, W. Xia, Z. Sun, C. Somsen, M. Muhler and W. Schuhmann, *Adv. Energy Mater.*, 2016, **6**, 1502313.
37 H. Liu, F. X. Ma, C. Y. Xu, L. Yang, Y. Du, P. P. Wang, S. Yang and L. Zhen, *ACS Appl. Mater. Interfaces*, 2017, **9**, 11634–11641.
38 G. Gardner, J. Al-Sharab, N. Danilovic, Y. B. Go, K. Ayers, M. Greenblatt and G. Charles Dismukes, *Energy Environ. Sci.*, 2016, **9**, 184–192.
39 K. Fan, H. Zou, Y. Lu, H. Chen, F. Li, J. Liu, L. Sun, L. Tong, M. F. Toney, M. Sui and J. Yu, *ACS Nano*, 2018, **12**, 12369–12379.
40 G. Zhang, G. Wang, Y. Liu, H. Liu, J. Qu and J. Li, *J. Am. Chem. Soc.*, 2016, **138**, 14686–14693.
41 X. Feng, W. Xing, L. Song and Y. Hu, *J. Mater. Chem. A*, 2014, **2**, 13299.
42 T. Pauporté, L. Mendoza, M. Cassir, M. C. Bernard and J. Chivot, *J. Electrochem. Soc.*, 2005, **152**, C49–C53.
43 M. Risch, F. Ringleb, M. Kohlhoff, P. Bogdanoff, P. Chernev, I. Zaharieva and H. Dau, *Energy Environ. Sci.*, 2015, **8**, 661–674.
44 H. Y. Wang, S. F. Hung, H. Y. Chen, T. S. Chan, H. M. Chen and B. Liu, *J. Am. Chem. Soc.*, 2016, **138**, 36–39.
45 X. Cui, Z. Xie and Y. Wang, *Nanoscale*, 2016, **8**, 11984–11992.
46 D. S. Dhawale, S. Kim, D.-H. Park, J.-H. Choy, S. S. Al-deyab, K. Ariga, E. Kim and A. Vinu, *ChemElectroChem*, 2015, **2**, 497–502.
47 X. Zhang, S. Liu, Y. Zang, R. Liu, G. Liu, G. Wang, Y. Zhang, H. Zhang and H. Zhao, *Nano Energy*, 2016, **30**, 93–102.
48 Y. Gao, L. Mi, W. Wei, S. Cui, Z. Zheng, H. Hou and W. Chen, *ACS Appl. Mater. Interfaces*, 2015, **7**, 4311–4319.
49 B. Hedman, P. Frank, S. F. Gheller, A. L. Roe, W. E. Newton and K. O. Hodgson, *J. Am. Chem. Soc.*, 1998, **110**, 3798–3805.
50 C. Hu, Q. Ma, S. F. Hung, Z. N. Chen, D. Ou, B. Ren, H. M. Chen, G. Fu and N. Zheng, *Chem*, 2017, **3**, 122–133.
51 D. F. Cao, O. A. Moses, B. B. Sheng, S. M. Chen, H. B. Pan, L. H. Wu, H. W. Shou, W. J. Xu, D. D. Li, L. R. Zheng, S. Q. Chu, C. S. Hu, D. B. Liu, S. Q. Wei, X. S. Zheng, Z. M. Qi, X. J. Wu, J. Zhang and L. Song, *Sci. Bull.*, 2020, DOI: 10.1016/j.scib.2020.09.037.
52 W. Ma, S. Xie, X. G. Zhang, F. Sun, J. Kang, Z. Jiang, Q. Zhang, D. Y. Wu and Y. Wang, *Nat. Commun.*, 2019, **10**, 892.
53 H. F. Wang, C. Tang, B. Q. Li and Q. Zhang, *Inorg. Chem. Front.*, 2018, **5**, 521–534.
54 B. Qiu, L. Cai, Y. Wang, X. Guo, S. Ma, Y. Zhu, Y. H. Tsang, Z. Zheng, R. Zhang and Y. Chai, *Small*, 2019, **15**, 1904507.
55 D. Zhou, Z. Cai, Y. Bi, W. Tiang, M. Luo, Q. Zhang, Q. Zhang, Q. Xie, J. Wang, Y. Li, Y. Kuang, X. Duan, M. Bajdich, S. Siahrostami and X. Sun, *Nano Res.*, 2018, **11**, 1358–1368.
56 Y. Shi, W. Du, W. Zhou, C. Wang, S. Lu, S. Lu and B. Zhang, *Angew. Chem., Int. Ed.*, 2020, **59**, 1–6.
57 C. X. Zhao, B. Q. Li, M. Zhao, J. N. Liu, L. D. Zhao, X. Chen and Q. Zhang, *Energy Environ. Sci.*, 2020, **13**, 1711–1716.
58 Y. Li, X. Du, J. Huang, C. Wu, Y. Sun, G. Zou, C. Yang and J. Xong, *Small*, 2019, **15**, 1901980.
59 J. Masa, S. Pinotek, P. Wilde, H. Antoni, T. Eckhard, Y. T. Chen, M. Muhler, U. P. Apfel and W. Schuhmann, *Adv. Energy Mater.*, 2019, **9**, 1900796.
60 B. Ni, T. He, J. O. Wang, S. Zhang, C. Ouyang, Y. Long, J. Zhuang and X. Wang, *Chem. Sci.*, 2018, **9**, 2762–2767.
61 X. Su, Y. Wang, J. Zhou, S. Gu, J. Li and S. Zhang, *J. Am. Chem. Soc.*, 2018, **140**, 11286–11292.
62 J. Yang, Z. Yang, L. H. Li, Q. Cai, H. Nie, M. Ge, X. Chen, Y. Chen and S. Huang, *Nanoscale*, 2017, **9**, 6886–6894.
63 J. Yang, H. Liu, W. N. Martens and R. L. Frost, *J. Phys. Chem. C*, 2009, **114**, 111–119.
64 L. Song, L. Ci, L. Lv, Z. Zhou, X. Yan, D. Liu, H. Yuan, Y. Gao, J. Wang, L. Liu, X. Zhao, Z. Zhang, X. Dou, W. Zhou, G. Wang, C. Wang and S. Xie, *Adv. Mater.*, 2004, **16**, 1529–1534.
65 B. Cui, H. Lin, J.-B. Li, X. Li, J. Yang and J. Tao, *Adv. Funct. Mater.*, 2008, **18**, 1440–1447.
66 C. Wei, R. R. Rao, J. Peng, B. Huang, I. E. L. Stephens, M. Risch, Z. J. Xu and Y. Shao-Horn, *Adv. Mater.*, 2019, **31**, 1806296.
67 T. Ressler, *J. Synchrotron Radiat.*, 1998, **5**, 118–122.
68 A. L. Ankudinov, B. Ravel, J. J. Rehr and S. D. Conradson, *Phys. Rev. B: Condens. Matter Mater. Phys.*, 1998, **58**, 7565–7576.

